Petroleum Science 23 (2026) 804–817

Contents lists available at ScienceDirect

Petroleum Science

journal homepage: www.keaipublishing.com/en/journals/petroleum-science

Original Paper

Modified Peng-Robinson equation of state for confined fluids: Critical pore size and phase behavior in shale nanopores

Hong-Xian Kuang [a], Zhou-Hua Wang [a,*], Na Jia [b], Han-Min Tu [a], Yun Li [c], Huang Liu [a], Ping Guo [a], Zi-Yan Wang [d]

[a] State Key Laboratory of Oil and Gas Reservoir Geology and Exploitation, Southwest Petroleum University, Chengdu, 610500, Sichuan, China
[b] Petroleum Systems Engineering, Faculty of Engineering and Applied Science, University of Regina, Regina, Saskatchewan, S4S 0A2, Canada
[c] Shenzhen Key Laboratory of Natural Gas Hydrates & Institute of Major Scientific Facilities for New Materials, Southern University of Science and Technology, Shenzhen, 518055, Guangdong, China
[d] School of Petroleum Engineering, Southwest Petroleum University, Chengdu, 610500, Sichuan, China

ARTICLE INFO

Article history:
Received 1 July 2025
Received in revised form
9 September 2025
Accepted 4 November 2025
Available online 8 November 2025

Edited by Meng-Jiao Zhou

Keywords:
Phase behavior
Equations of state
Fluid adsorption
Wettability
Shale condensate gas

ABSTRACT

Shale reservoirs are dominated by nanopores, where wall-fluid adsorption and anomalous fluid intermolecular interactions lead to substantial deviations from conventional equation of state (EOS) predictions. This study proposes a modified Peng-Robinson equation of state (m-PR EOS) that incorporates two innovative key corrections: (1) a refined molar volume term accounting for wall-fluid adsorption effects; and (2) introduction of the contact angle in the attractive term to rectify anomalous fluid intermolecular interactions. The m-PR EOS quantitatively captures the shifts in critical properties of confined hydrocarbons and pioneeringly integrates critical pore size determination, identifying confinement thresholds for pure hydrocarbons. The critical pore radii of methane were determined as 18.62 nm (based on temperature shift) and 51.33 nm (based on pressure shift). The analysis reveals that hydrocarbons with larger Lennard-Jones molecular sizes exhibit larger critical pore sizes and greater deviations in critical properties at the same confinement scale. The model validated with binary hydrocarbons was applied to simulate pore-size-dependent phase behavior in shale condensate systems and Constant Composition Expansion experiments. Results demonstrate that reducing pore size causes phase envelope to contract towards the lower-left quadrant in the *P-T* phase diagram, with accelerated contraction rates. Constant Composition Expansion simulations show that the retrograde condensation volume curve exhibits a similar contraction trend as the phase envelope. By incorporating wettability effects, the m-PR EOS model extends its applicability to a wide range of reservoirs. The m-PR EOS provides a thermodynamic foundation for accurately predicting nanoscale phase behavior and optimizing condensate recovery in unconventional reservoirs.

1. Introduction

As an unconventional resource, shale oil and gas offer abundant reserves and significant development potential, presenting promising opportunities for future exploitation (Caineng et al., 2019; Milad et al., 2021; Xu et al., 2022). According to statistical results, the pore sizes of China shale oil and gas reservoirs were mainly in the range of 5–200 nm (Jia et al., 2012; Kuila and Prasad, 2013; Liu et al., 2024). Such nanometer-scale pores are the core storage space and flow path in unconventional oil and gas reservoirs and have a significant impact on the presence, flow, and production of oil and gas (Wu et al., 2021). A comprehensive understanding of the phase behavior of hydrocarbon fluids in nanopores enhances our understanding of the dynamic changes of shale oil and gas during the development process.

In nanoscale spaces, the strong interactions between fluid molecules and the pore walls result in a significant amount of oil and gas molecules being tightly adsorbed onto the walls of the nanoscale pores, forming an adsorbed layer with a specific

* Corresponding author.
E-mail address: wangzhouhua@126.com (Z.-H. Wang).
Peer review under the responsibility of China University of Petroleum (Beijing).

https://doi.org/10.1016/j.petsci.2025.11.010

thickness. Numerous studies (Ma and Jamili, 2016; Jin and Nasrabadi, 2016; Vishnyakov and Neimark, 2009; Yu et al., 2022) have demonstrated that there were significant differences in properties between the adsorbed fluid molecules near the wall and the free fluid molecules in the pore center, which can further affect the phase behavior and critical properties of the fluid in nanopores. Additionally, researchers (Pang et al., 2019; Tian et al., 2017; Yu et al., 2022) have found that the density and intermolecular potential energy of free fluid molecules in nanoscale spaces also differed from those in bulk phases, reflecting the interactions received from the nanoscale environment. The adsorption of fluid molecules onto the walls and the anomalous intermolecular interactions between fluid molecules collectively influence the thermophysical properties of fluids in nanopores.

Previous studies deeply explored the characteristics and behaviors of fluid in nanoscale spaces through various methods, including experimental approaches (Alfi et al., 2016; Tan et al., 2019), molecular simulations (Santos et al., 2018; Tian et al., 2018), and density functional theory (DFT) (Li et al., 2014). Adsorption-desorption methods, differential scanning calorimetry (DSC), diffusion methods, and nanofluidic channel chip experiments are the principal experimental techniques for studying fluid phase states in confined spaces (Liu and Zhang, 2019). Yun et al. (2002) and Russo et al. (2012) utilized adsorption-desorption methods to measure the critical points of single alkane components in nanoscale spaces. These findings confirmed that confined fluids' saturation pressure and critical conditions are lower than those at the bulk phase. Researchers (Luo et al., 2016, 2018; Qiu et al., 2018) used DSC to find that the phase transition points of simple hydrocarbon and their mixtures in confined spaces are lower than those for bulk phase fluids, but the artificially preset temperature change rate influences the test results. The diffusion method (Zeigermann et al., 2009) for fluids in nanoscale pore spaces determines their critical temperature by establishing the relationship between the diffusion coefficients and temperature. Similar to the DSC method, the rate of temperature change influences the accuracy of the diffusion method results; only a range is allowed to determine the critical temperature. Researchers (Alfi et al., 2016; Parsa et al., 2015; Wang et al., 2014) used the nanofluidic channel chip experimental method to explore the phase behavior of simple hydrocarbon fluids in confined spaces and found that the size of the confined space is the main factor influencing phase behavior, with the suppressed evaporation behavior of the liquid phase. This method is a direct measurement approach, with phase transition points less affected by external factors and leverages actual reservoir temperature and pressure conditions; however, it requires a high operational cost and complex technical implementation, making it challenging for widespread usage.

Molecular simulation techniques provide a direct means to describe adsorption and explain the involved microscopic mechanisms. Jang and Chung (2019) used the Grand Canonical Monte Carlo (GCMC) method to simulate the adsorption of methane and carbon dioxide in illite slits, suggesting that van der Waals forces are universally present between gas-solid molecules. Zhu et al. (2016) used molecular simulation with DFT to study the adsorption mechanism of methane, revealing that the interaction between methane and kerogen is primarily governed by van der Waals forces and methane adsorption in kerogen is a physical process. Some researchers (Wang et al., 2015a; Wang et al., 2015b) investigated the adsorption behavior of confined n-heptane, heptane, and their mixtures in slit nanospace, revealing the presence of multiple adsorption layers with the number of layers depended on pore size and fluid composition, and the preference of pore walls favoured the adsorption of heavier hydrocarbons than lighter ones. Regarding the changes in critical properties of fluids in nanoscale spaces, some researchers (Jin and Nasrabadi, 2016; Vishnyakov and Neimark, 2009; Yu et al., 2022) utilized the GCMC method to generate the phase diagram of confined fluids in slit pores, indicating that compared to bulk phase states, the critical temperature of methane and pentane in confined spaces was lower, while the critical density was higher. These studies (Jin and Nasrabadi, 2016; Vishnyakov and Neimark, 2009; Yu et al., 2022) examined the phase behavior of methane, ethane, and their mixtures confined in graphite sheets using GCMC simulations. They found that the critical temperature and critical pressure of confined methane and ethane were reduced, while the critical density increased. Jin et al. (2013) examined the phase behavior and fluid properties of mixtures of methane, n-butane, and n-octane and observed that as pore size decreased, the envelope of the phase diagram shrank, leading to reduced critical properties and increased heavy component presence. Mota and Esteves (2007) and Jiang et al. (2004) investigated the phase transitions of pure n-alkanes (ethane, propane, and n-butane) and pure propane in carbon nanotubes. They concluded that the critical temperature decreased and the critical density increased in nanoscale spaces.

Based on the calculated Helmholtz free energy using a van der Waals mean field model for a confined Lennard-Jones fluid in a nanopore, Zarragoicoechea and Kuz (2002) proposed equations for quantifying the critical temperature and critical pressure shifts. However, their calculation assumed inert walls, which neglected the fluid-wall interactions. Zhang et al. (2019c) extended Zarragoicoechea and Kuz's work to establish new thermodynamic formulations based on four classical cubic equation of states (van der Waals, Redlich-Kwong, Soave-Redlich-Kwong, and Peng-Robinson equation of state), which not only considered molecular interactions based on Lennard-Jones potential but also accounted for molecular-wall interactions through a potential well model. Cui et al. (2018) proposed a model that introduced an effective molecular volume coefficient (ε) and modified the molar volume term by reducing the mole number of free fluid molecules due to adsorption, resulting in a new corrected Peng-Robinson equation of state (PR EOS). However, this model assumed that fluid molecules in nanoscale spaces are rigid spheres arranged uniformly on the wall, forming an adsorbed layer, which is too idealistic. Fu et al. (2023) modified the PR EOS by introducing a new parameter based on the relative cross-sectional perimeter of the pore relative to the cylindrical-shaped cross-section, and also considered the adsorption effects of surfaces with varying geometries. Song et al. (2020) proposed a new corrected PR EOS based on the modification of the molar volume for nanoscale fluid; they developed a physical model without assuming adsorbed molecules as rigid spheres or defining their arrangement but incorporated properties like the number of molecular layers and density of the adsorbed layer, and introduced a new parameter to represent the thickness and density of the adsorbed layer quantitatively. Wang et al. (2022) implemented a similar model and method to correct the Soave-Redlich-Kwong equation of state (SRK EOS) and achieved good predictive results for phase states in nanoscale spaces under various conditions. It is noteworthy that correcting the molar volume by neglecting the contribution of adsorbed molecules may lead to an overestimation of the molar volume; however, due to the influence of nanoscale confinement, adsorbed fluid molecules tend to arrange more closely. This closer arrangement results in a shorter overall average free path of the fluid molecules, enhancing intermolecular interactions and ultimately increasing fluid density while decreasing molar volume.

Moreover, it should be noted that confined fluids exhibit pronounced finite-size scaling effects near the critical point. When the

correlation length becomes comparable to the pore radius R_p, confinement strongly affects critical parameters such as the critical temperature, critical pressure and critical density; this behavior can be explained by finite-size scaling theory. At the same time, nonclassical phenomena—including density variations near solid walls, the thickness of the adsorbed layer, and critical wetting transitions—also exert a significant influence on the thermodynamic behavior of confined fluids. These effects lie beyond the scope of traditional classical models; therefore, finite-size and other nonclassical effects should be given special consideration when studying the phase behavior of fluids in nanopores.

Regarding the differences in fluid phase behavior between nanoscale spaces and bulk conditions, some scholars focused on fluid molecule adsorption on pore walls to adjust the molar volume (Cui et al., 2018; Song et al., 2020; Wang et al., 2022). Others concentrated on the abnormal interactions between fluid molecules induced by nanoscale confinement (Zarragoicoechea and Kuz, 2004; Zhang et al., 2019c). While these foundational studies remain valid, emerging evidence demonstrates significant deviations in both adsorbed and free fluid molecule behavior within nanoconfinement compared to bulk phase conditions (Jin and Nasrabadi, 2016; Vishnyakov and Neimark, 2009; Xing et al., 2021; Yu et al., 2022). Under equivalent thermal conditions, the confined system exhibits pronounced spatial density variations, in sharp contrast to the homogeneous bulk phase. This fundamental distinction necessitates explicit consideration of two critical factors in thermodynamic modeling: 1) wall adsorption effects modifying molecular distributions, and 2) the different wettability conditions and fluid-fluid molecular interactions governing phase transitions—both essential for accurate characterization of confined fluid phase behavior.

This study introduces a new unified thermodynamic framework and a modified Peng-Robinson EOS that, innovatively, jointly account for pore size, wettability, and adsorption to predict the phase behavior of hydrocarbons at the nanoscale with unprecedented accuracy. It establishes and validates new mixing rules for further calculating the phase behavior of mixed hydrocarbon fluids in nanoscale shale reservoirs. The work proposes a novel correction method for the molar volume in nanoscale spaces, demonstrating how adsorbed molecules can be converted into free molecules, and incorporates the contact angle (between hydrocarbon fluids and pore walls) into the attraction parameter a to enable the transformation of free molecules into bulk molecules. A coherent, self-consistent set of corrections is proposed for converting confined nanoscale fluid molecules into bulk molecules, thereby enabling precise prediction of phase envelopes, shifts in critical properties, and critical pore sizes in complex, heterogeneously wetted shale nanopores. Based on experimental data of bulk phase, this model is then applied to predict *P-T* phase diagrams and CCE curves under various pore-size and wettability conditions, offering crucial guidance for mitigating retrograde condensation damage and optimizing condensate-gas recovery.

2. Methodology

2.1. Modification for the molar volume of nano-confined fluids

The physical model for modifying the EOS was previously proposed aiming to convert the fluid phase in nanopores to a bulk phase by modifying the adsorption effect of the nanopore walls on fluid molecules. In this modification process, both models independently use the equation $V'_m = V_m n_t/(n_t - n_a)$ to correct the molar volume, where n_a is the number of adsorbed layer molecules, n_t is the total number of pore molecules, V'_m is the corrected molar volume, and V_m is the original molar volume of the pore before the correction. This equation ignores the fluid molecules adsorbed on the pore walls and treats the free molecules as the total number of molecules in all nanopores, as shown in Fig. 1. This correction leads to a higher value of molar volume V'_m compared to that of the original molar volume V_m. However, it is known that the adsorption of molecules on the pore walls and the anomalous intermolecular interactions between fluid molecules in the nanopores increase the fluid density and reduce the molar volume. When the pore size is very small and n_a and n_t values are very close, this causes an extremely large value of $n_t/(n_t - n_a)$ and a much larger V'_m than V_m. As a consequence, the smaller the nanopore, the greater the inappropriateness of this assumption will be.

As a result, the method proposed for calculating the molar volume in this study is

$$V'_m = \frac{n_t}{(n_t - n_a) + \frac{\rho_f}{\rho_a} n_a} V_m \tag{1}$$

Here, the adsorbed molecules are converted into free molecules according to their density ratio. This step focuses on accounting for the adsorption effect of the pore walls on the fluid molecules. With more manipulation, the modified molar volume is expressed as

$$V'_m = \frac{V_m n_t}{(n_t - n_a) + \frac{\rho_f}{\rho_a} n_a} = \frac{V_m}{1 + \mu\xi} \tag{2}$$

$$\mu = \frac{n_t - n_f}{n_t} = 1 - \frac{\rho_f (R_p - \delta)^2}{\rho_t R_p^2} \tag{3}$$

$$\xi = \frac{\rho_f}{\rho_a} - 1 \tag{4}$$

where μ reflects the percentage of adsorbed molecules relative to the total number of molecules in the nanopore, and ξ reflects the correction to the adsorbed layer density. When the pore radius R_p is much larger than the adsorbed layer thickness δ, then $(R_p - \delta)^2 \approx R_p^2$ and $\rho_f \approx \rho_t$, resulting in $\mu \approx 0$ and $V'_m \approx V_m$. Under these conditions, the corrected EOS naturally reduces to the traditional EOS for the bulk phase. Fig. 2 visually illustrates the physical process by which Eq. (2) transforms adsorbed molecules into free molecules. The new, more physically justified molar volume correction given by Eq. (2) is incorporated into the equation of state as Eq. (8), enabling the modified PR EOS to predict the effect of adsorption on the critical properties of hydrocarbon fluids. To further correct the phase behavior of confined molecules toward bulk phase behavior, the attraction parameter a in the original EOS is adjusted to account for the anomalous intermolecular interactions in nanopores. By combining the new molar volume correction with the adjusted attraction parameter a, we developed a modified EOS that can describe fluid phase behavior in nanopores.

Fig. 2 shows that free molecules and bulk molecules still exhibit a density difference, which arises from a pressure imbalance at the meniscus caused by capillary pressure. From the expression for capillary pressure, the contact angle is an important factor that influences capillary pressure. Capillary pressure applies an additional force to the fluid at the three-phase interface in nanoscale pores, changing the intermolecular spacing and causing the attractive term in conventional equations of state to deviate from the actual intermolecular attraction in nanoscale pores. Related studies showed that variations in contact angle significantly influence the phase behavior of fluids in nanopores (Feng et al., 2021; Wang et al., 2025). The

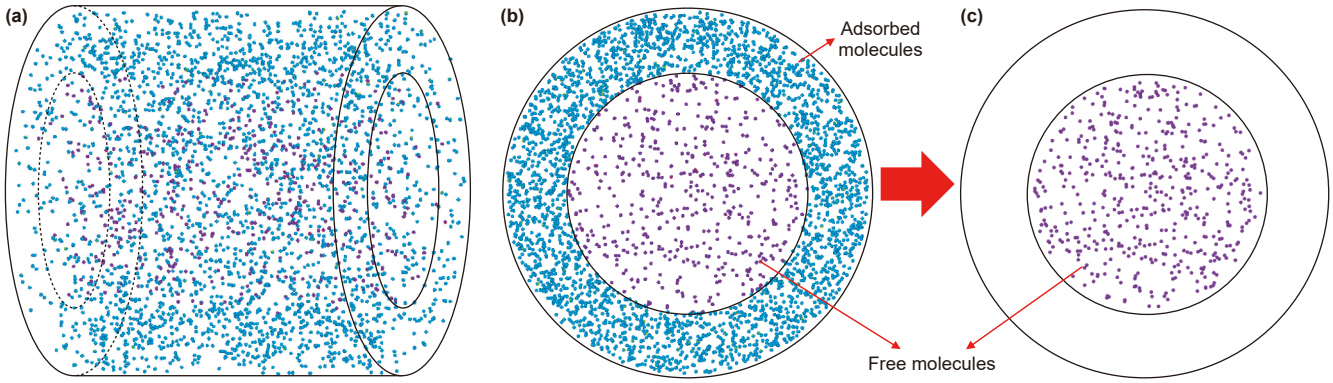

Fig. 1. The physical model for the molar volume correction proposed by Song et al. (2020).

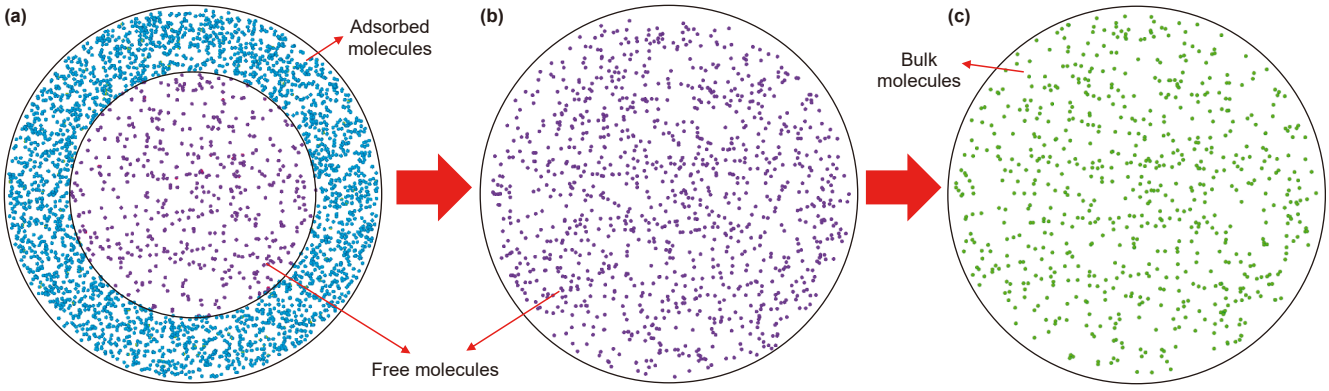

Fig. 2. Physical model of the modified equation of state proposed in this study.

transition from Fig. 2(b) and (c) is achieved by incorporating the contact angle θ into the attraction parameter a in Eq. (7) (Feng et al., 2021), thereby correcting for the effects of contact angle and capillary pressure on phase behavior. This correction reconciles the differences between the intermolecular forces among free molecules and those among bulk molecules, effectively converting free molecules into bulk molecules. Consequently, the molecular density within the modeled physical space undergoes corresponding changes, reflecting adjustments to the anomalous intermolecular interactions of fluids in nanoscale spaces.

2.2. Adsorption layer thickness

The adsorption of fluid molecules on pore walls in nanopores is a typical phenomenon, and calculating the adsorption thickness through molecular simulations or experimental methods is a time-consuming and labour-intensive task (Dubinin, 1960; Foo and Hameed, 2010; Jin and Nasrabadi, 2016; Yu et al., 2022). The adsorption thickness is particularly important for understanding the molecular distribution characteristics in nanopores, as it helps scholars better understand the occurrence and proportion of various molecules in nanopores. Therefore, the expression of the adsorption layer thickness is related to the dimensionless radius σ_{LJ}/R_p proposed by Zhang et al. (2019a), as shown in Eq. (5). It fits well with the method used in this study to calculate the degree of critical property shifts.

$$\delta = \frac{m}{\ln(R_p/\sigma_{LJ})} + n\left(\frac{\sigma_{LJ}}{R_p}\right) \tag{5}$$

$$m = -8.3140 \times 10^{-14}M^2 + 2.0475 \times 10^{-11}M + 3.0886 \times 10^{-11} \tag{5-a}$$

$$n = -6.3565 \times 10^{-14}M^2 + 3.1550 \times 10^{-11}M - 5.8538 \times 10^{-10} \tag{5-b}$$

where m and n are coefficients and M is the molecular weight. It should be noted that the formulations of m and n are obtained from the non-linear least-square method (Zhang et al., 2019a). σ_{LJ} is the Lennard-Jones molecular size parameter, nm; each alkane molecule has a fixed value for its σ_{LJ} (Zhang et al., 2018).

Adsorption-density distribution plots from relevant studies (Dong et al., 2022; Wang et al., 2015) indicate that, within the same nanoscale pore, the adsorption layer thickness δ for a given alkane is similar in pure hydrocarbon and mixed hydrocarbon systems. The principal difference is that the density of each alkane within the adsorption layer can vary substantially. In complex hydrocarbon mixtures, because more alkane species are present, the amount of each alkane in the adsorption layer correspondingly decreases. Therefore, the expression for adsorption layer thickness δ given in Eq. (5) is also applicable to complex hydrocarbon mixtures.

2.3. Solution for modified PR EOS

The m-PR EOS in this study is based on the conventional PR EOS (Peng and Robinson, 1976):

$$P=\frac{RT}{V-b}-\frac{\alpha a}{V(V+b)+b(V-b)} \tag{6}$$

$$\alpha=\left[1+\lambda\left(1-\sqrt{T_r}\right)\right]^2 \tag{6-a}$$

$$\lambda=0.315+1.6\omega-0.166\omega^2 \tag{6-b}$$

where α is the temperature-dependent parameter. T_r is the reduced temperature and $T_r = T/T_c$. The parameter λ is determined by the molecular acentric factor ω.

The m-PR EOS introduces the corrected molar volume term (V'_m) and attraction parameter (a') for nano-confined fluids into the conventional PR EOS, as follows:

$$P=\frac{RT}{V'_m-b}-\frac{\alpha a'}{V'_m(V'_m+b)+b(V'_m-b)} \tag{7}$$

Therefore,

$$P=\frac{RT}{\frac{V_m}{1+\mu\xi}-b}-\frac{\alpha a\times\left(1-C\ln\left(\frac{180}{\theta}\right)\frac{\sigma_{LJ}}{R_p}\right)}{\frac{V_m}{1+\mu\xi}\left(\frac{V_m}{1+\mu\xi}+b\right)+b\left(\frac{V_m}{1+\mu\xi}-b\right)} \tag{8}$$

The critical isotherm shows a turning point existing at the critical point,

$$\left(\frac{\partial P}{\partial V}\right)_{T=T_c}=\left(\frac{\partial^2 P}{\partial V^2}\right)_{T=T_c}=0 \tag{9}$$

When $T = T_c$, $\alpha = 1$. By substituting Eq. (9) into Eq. (8), the parameters a', a and b can be represented as follows:

$$a'=0.45724\frac{R^2T_c^2}{P_c} \tag{10}$$

$$a'=a\times\left(1-C\ln\left(\frac{180}{\theta}\right)\frac{\sigma_{LJ}}{R_p}\right) \tag{11}$$

$$a=0.45724\frac{R^2T_c^2}{P_c\left(1-C\ln\left(\frac{180}{\theta}\right)\frac{\sigma_{LJ}}{R_p}\right)} \tag{12}$$

$$b=0.07780\frac{RT_c}{P_c}(1+\mu\xi) \tag{13}$$

where P_c is critical pressure and R is the ideal gas constant. The detailed calculations are presented in Appendix A.

As previously noted, correcting the molar volume term is crucial for adjusting the parameter b. Appendix A outlines the detailed derivation of parameters a' and b, along with the formulation for the fugacity coefficient in both the vapor and liquid phases of pure hydrocarbon and mixed hydrocarbon systems.

Consequently, the critical pressure and temperature can be expressed as follows:

$$P_{c\,m}=0.01324\frac{a'}{b^2}(1+\mu\xi)^2 \tag{14}$$

$$T_{c\,m}=0.17015\frac{a'}{bR}(1+\mu\xi) \tag{15}$$

where P_{cm} and T_{cm} represent the modified critical pressure and critical temperature from the m-PR EOS. Thus, the dimensionless shifts in critical properties in confined space are defined as follows:

$$\Delta P_c=\frac{P_c-P_{c\,m}}{P_c}=1-\left(1-C\ln\left(\frac{180}{\theta}\right)\frac{\sigma_{LJ}}{R_p}\right)(1+\mu\xi)^2,\ \Delta P\in\left[0,1\right) \tag{16}$$

$$\Delta T_c=\frac{T_c-T_{c\,m}}{T_c}=1-\left(1-C\ln\left(\frac{180}{\theta}\right)\frac{\sigma_{LJ}}{R_p}\right)(1+\mu\xi),\ \Delta T\in\left[0,1\right) \tag{17}$$

The above two equations establish a quantitative relationship between the adsorption phenomenon and the induced critical shifts in confined fluids.

2.4. Correlation for critical temperature shift

In previous studies, most scholars consistently accepted that the size of fluid molecules, represented by the Lennard-Jones molecular size parameter σ_{LJ}, and the size of the nanopores R_p are important factors influencing the shift in critical properties of fluid molecules. Therefore, they often chose the dimensionless pore size σ_{LJ}/R_p as the key input parameter and investigate its effects on both ΔP_c and ΔT_c, as shown in Tables 1 and 2. The expressions for ΔT_c and ΔP_c derived from the m-PR EOS were fit and validated. Forty-five sets of experimental or simulation data were used for fitting as shown in Fig. 3, and twenty-six sets for validation of ΔT_c.

$$\Delta T_c=-0.4848\left(\frac{\sigma_{LJ}}{R_p}\right)^2+1.313\left(\frac{\sigma_{LJ}}{R_p}\right)-0.025,\ \Delta T\in\left[0,1\right) \tag{18}$$

By substituting ΔT_c into the expression for ΔP_c, one obtains:

$$\Delta P_c=1-\left(1-C\ln\left(\frac{180}{\theta}\right)\frac{\sigma_{LJ}}{R_p}\right)(1-\Delta T_c)^2=1-\left(1-C\ln\left(\frac{180}{\theta}\right)\frac{\sigma_{LJ}}{R_p}\right)\left(\left(0.4848\left(\frac{\sigma_{LJ}}{R_p}\right)^2-1.313\frac{\sigma_{LJ}}{R_p}+1.025\right)^2,\ \Delta P\in\left[0,1\right)\right) \tag{19}$$

Previous studies have rarely specifically focused on fitting the expression for ΔP_c. However, to enhance the accuracy of critical pressure shift predictions, it is essential that the ΔP_c expression be carefully refined within the physical model presented in this study. Therefore, special attention must be paid during the refining

Table 1
Summary of analytic formulas for critical temperature shift.

Critical temperature shift	Reference
$\Delta T_c = 0.9409\frac{\sigma_{LJ}}{R_p} - 0.2415\left(\frac{\sigma_{LJ}}{R_p}\right)^2$	Zarragoicoechea and Kuz (2004)
$\Delta T_c = 0.8493 \times \left(\frac{R_p}{\sigma_{LJ}}\right)^{-1.241} + 0.015$	Jin et al. (2013)
$\Delta T_c = 3.374 \times \left(\frac{R_p}{\sigma_{LJ}}\right)^{-1.637}$	Yang et al. (2019)
$\Delta T_c = 0.7197\frac{\sigma_{LJ}}{R_p} - 0.0758\left(\frac{\sigma_{LJ}}{R_p}\right)^2$	Zhang et al. (2019b)
$\Delta T_c = 0.6794 \times \left(\frac{\sigma_{LJ}}{R_p}\right)^{0.7878}$	Song et al. (2020)
$\Delta T_c = \begin{cases} 0.961\left(\frac{R_p}{\sigma_{LJ}}\right)^{-0.892}, & 0 < \ln\left(\frac{R_p}{\sigma_{LJ}}\right) < 2 \\ 29.400\left(\frac{R_p}{\sigma_{LJ}}\right)^{-2.506}, & \ln\left(\frac{R_p}{\sigma_{LJ}}\right) \geqslant 2 \end{cases}$	Wang et al. (2022)

Table 2
Summary of analytic formulas for critical pressure shift.

Critical pressure shift	Reference
$\Delta P_c = 0.9409\frac{\sigma_{LJ}}{R_p} - 0.2415\left(\frac{\sigma_{LJ}}{R_p}\right)^2$	Zarragoicoechea and Kuz (2004)
$\Delta P_c = 1.8 \times \left(\frac{R_p}{\sigma_{LJ}}\right)^{-0.775}$	Jin et al. (2013)
$\Delta P_c = 0.7197\frac{\sigma_{LJ}}{R_p} - 0.0758\left(\frac{\sigma_{LJ}}{R_p}\right)^2$	Zhang et al. (2019b)
$\Delta P_c = 1.3588 \times \left(\frac{\sigma_{LJ}}{R_p}\right)^{0.7878} - 0.4616 \times \left(\frac{\sigma_{LJ}}{R_p}\right)^{1.3588}$	Song et al. (2020)
$\Delta P_c = \begin{cases} 1 - \left[1 - 0.961\left(\frac{R_p}{\sigma_{LJ}}\right)^{-0.892}\right]^2, & 0 < \ln\left(\frac{R_p}{\sigma_{LJ}}\right) < 2 \\ 1 - \left[1 - 29.400\left(\frac{R_p}{\sigma_{LJ}}\right)^{-2.506}\right]^2, & \ln\left(\frac{R_p}{\sigma_{LJ}}\right) \geqslant 2 \end{cases}$	Wang et al. (2022)
$\Delta P_c = 1 - \left(0.4848\left(\frac{\sigma_{LJ}}{R_p}\right)^2 - 1.313\left(\frac{\sigma_{LJ}}{R_p}\right) + 1.025\right)^2$	This study without modified a

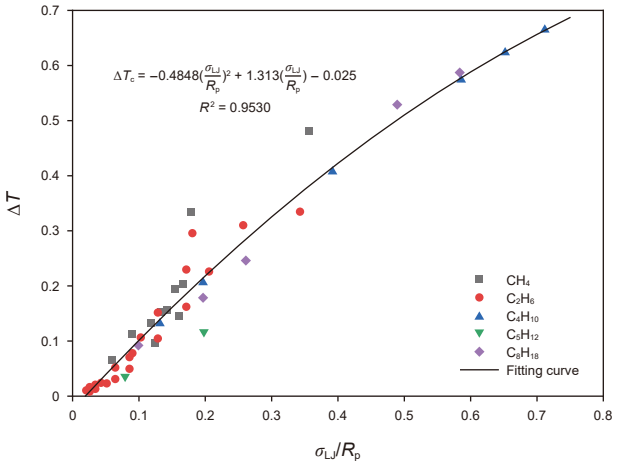

Fig. 3. Correlation for critical temperature shift with the data points from the literature (Li et al., 2014; Morishige et al., 1997; Pitakbunkate et al., 2016; Singh and Singh, 2011; Singh et al., 2009; Vishnyakov et al., 2001; Zarragoicoechea and Kuz, 2002).

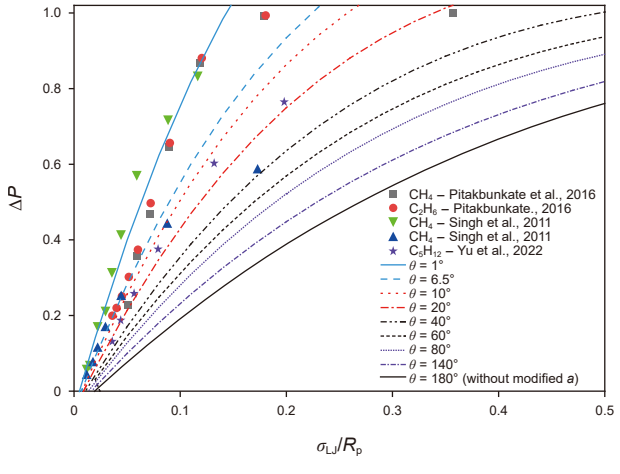

Fig. 4. Comparison and validation of the ΔP_c expression before and after modifying a.

process. Because the ΔP_c data are widely scattered, the R^2 value of the fitting equation remains low, regardless of the equation form. Several key factors that may contribute to this situation are: (i) Nanopore walls used by different researchers are composed of various substances (such as inorganic minerals like graphite and silica versus organic coatings containing methyl or hydroxyl groups), which can alter solid-liquid interfacial potential energies;

(ii) The computational methods based on different theoretical frameworks (such as DFT, molecular dynamics simulations (MD), and GCMC) may introduce discrepancies in the results; (iii) In molecular simulations, ΔP_c value deviations are highly sensitive to parameterization choices, particularly the cutoff radius and dispersion correction terms in Lennard-Jones potential calculations. This study drew on the work of Feng et al. (2021) by introducing the contact angle θ, which significantly improved the m-PR EOS's accuracy in predicting the critical pressure of nanoconfined fluids. The optimized critical pressure predictions are shown in Fig. 4.

Fig. 4 shows the magnitude of the shift in critical temperature for different contact angles. When $\theta = 180°$, Eq. (11) reduces to $a' = a$; this physically means that only adsorption is considered and the effect of the contact angle is neglected. By comparing the curve for $\theta = 180°$ with the other curves, the relative contributions of capillary pressure and adsorption can be determined.

Under reservoir conditions, highly mature shales often display hydrophobicity (Arif et al., 2021). At the oil–water–shale three-phase interface, oil contact angles typically range from 25° to 80° (Arif et al., 2017; Arif et al., 2021; Pan et al., 2018; Wang et al., 2025). On untreated, water-free shale samples, oil at the oil–gas–shale three-phase interface spreads rapidly on the dry surface (contact angle approaching 0°) (Bhutto et al., 2022). After analyzing the complexity of the above ΔP_c data distribution, this study selected $\theta = 6.5°$, which reflects the overall trend of ΔP_c for water-free hydrocarbon fluids shown in Fig. 4. Here, $\theta = 6.5°$ is presented merely as an illustrative example; readers should select the θ value appropriate for other reservoirs based on actual test results. From the refining results, it can be obtained that:

$$\begin{aligned}\Delta P_c &= 1-\left(1-1.344\ln\left(\frac{180}{6.5}\right)\frac{\sigma_{LJ}}{R_p}\right)(1-\Delta T_c)^2\\ &= 1-\left(1-4.4636\frac{\sigma_{LJ}}{R_p}\right)\left(0.4848\left(\frac{\sigma_{LJ}}{R_p}\right)^2-1.313\frac{\sigma_{LJ}}{R_p}+1.025\right)^2,\\ \Delta P &\in \left[0,1\right)\end{aligned} \tag{20}$$

Taking methane as an example, at the vertical coordinate $\Delta P_c = 0$, $\sigma_{LJ}/R_p = 0.006955$, and thus $R_p = 51.33$ nm, it indicates that for methane, when pore radius $R_p < 51.33$ nm, the critical pressure of the nanopore starts to shift.

Thus, the complete formulation of the m-PR EOS and its parameters have been derived. When the pore size is smaller than the critical radius, this equation can predict the shift in critical properties. As R_p continuously increases, the shift in critical properties tends to approach zero, and the m-PR EOS returns to its traditional form.

2.5. Experimental procedure of Constant Composition Expansion (CCE)

A Constant Composition Expansion (CCE) experiment was used to determine the dew-point pressure at 411.15 K. The recombined condensate gas sample was loaded into the PVT cell, heated to 411.15 K, and equilibrated at a pressure above the expected dew point (single-phase region). With temperature held constant, the pump was used to incrementally expand the cell volume, thereby lowering pressure in small steps. After each expansion step the system was stirred and allowed to equilibrate (pressure and temperature stabilized). The pressure and total volume were recorded continuously. The dew-point pressure was identified as the pressure at which the first liquid condensate appeared in the cell window. The criterion for dew-point detection followed standard practice: visual observation of the incipient liquid phase. At each step the emergent liquid volume (if any) was noted. In summary, pressure was decreased by controlled volume expansion until a drop of condensate was seen, marking the dew point. Continued to expand the cell volume, reducing the pressure in 2 MPa increments, until the sample volume reached three times the volume at the dew point pressure.

3. Results and discussions

3.1. Model validation and comparison

To verify the accuracy of the developed expression of critical temperature shift, the fitted expressions of ΔT_c and ΔP_c are compared with those obtained from other literature (Song et al., 2020; Wang et al., 2022; Yang et al., 2019; Zarragoicoechea and Kuz, 2004; Zhang et al., 2019b), as summarized in Tables 1 and 2. The ΔT_c expressions from other articles intersect the coordinate axes at (0, 0). This indicates that whenever pores are present, a corresponding critical temperature shift occurs within them. This differs from the consensus of the critical pore size for confined effects, which is defined as the threshold pore size at which nanoconfinement induces shifts in critical properties. Jin et al. (2013)'s ΔT_c fitting formula intersects the y-axis at (0, 0.015), reflecting that there is also a critical temperature shift in the bulk phase space, which differs from the views of other studies.

The ΔT_c expression developed in this study intersects the x-axis at (0.019176, 0). This suggests that the pore radius at which methane begins to experience confined effects is $R_p < 18.62$ nm, in close agreement with the conclusion of the data providers (Li et al., 2014; Morishige et al., 1997; Pitakbunkate et al., 2016; Singh and Singh, 2011; Singh et al., 2009; Vishnyakov et al., 2001; Zarragoicoechea and Kuz, 2002). By analyzing the physical significance of the ΔT_c expressions, this study finds that some of the fitted equations do not fully align with the theoretical interpretations and conclusions reported in the literature that serves as the data source as shown in Fig. 5. This highlights the importance of ensuring that these equations are used only when their physical interpretation remains reasonable.

Fig. 6 presents the additional fitted curves listed in Table 2. All of these curves pass through the origin (0, 0), indicating that the critical pressure shift does not have a critical pore size. In other

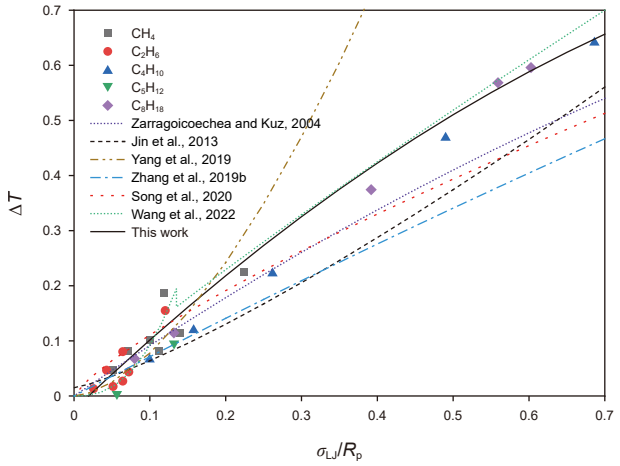

Fig. 5. Comparison of critical temperature shift calculated from different models using the data points.

words, as R_p approaches infinity, the critical pressure shift gradually tends to approach zero. A comparison of Figs. 4 and 6 shows that models ignoring the contact angle cannot accurately predict the experimentally measured critical pressure data for different wall materials. In this study, the contact angle θ is introduced into the PR EOS, yielding the m-PR EOS, which can predict the critical pressure shifts of fluids in pores with varying wettability.

3.2. Phase diagram calculation of pure hydrocarbon fluids

The m-PR EOS can be applied to the flash calculations for both pure hydrocarbon and multi-component hydrocarbon fluids, as well as the bubble-point and dew-point calculations. This study calculates the *P-T* phase diagram of pure hydrocarbon fluids (using methane as an example) at varying nanopore sizes. As shown in Fig. 7, the *P-T* phase diagram contracts toward the lower-left quadrant as the pore size decreases, with the contraction becoming more pronounced at smaller radii. The diagram reflects the variation pattern in the critical properties of pure hydrocarbon fluids, which aligns with the conclusions of numerous references (Li et al., 2014; Morishige et al., 1997; Pitakbunkate et al., 2016; Singh and Singh, 2011; Singh et al., 2009; Vishnyakov et al., 2001; Zarragoicoechea and Kuz, 2002).

Fig. 8 compares the critical temperature and pressure shifts of methane, pentane, and decane. By analyzing the effect of the Lennard-Jones molecular size σ_{LJ} on the monotonicity of the expressions for ΔT_c and ΔP_c, we find that when the Lennard–Jones molecular size is smaller than the nanopore size, larger molecular sizes lead to greater values of ΔT_c and ΔP_c. The trends in critical-property shifts for different alkanes shown in Fig. 8 provide important support for this conclusion, visually demonstrating that the degree of the shift in critical properties increases with σ_{LJ}. Overall, at a given pore size, heavier hydrocarbons exhibit greater shifts in critical temperature and pressure than lighter hydrocarbons. Moreover, the critical pore size for heavier hydrocarbons is larger than that for lighter counterparts. However, this pattern does not apply to propane, as evidenced by the variation trends in σ_{LJ} (Yu and Gao, 2000; Zhang et al., 2018), since the value of σ_{LJ} for propane is smaller than that for methane and ethane.

This study pioneers the integration of the critical pore size into the computational framework of the m-PR EOS to quantitatively determine the threshold pore size at which critical temperature and pressure shifts occur for various pure hydrocarbon species. Taking a contact angle $\theta = 6.5°$ as an example, Fig. 8 also confirms these conclusions:

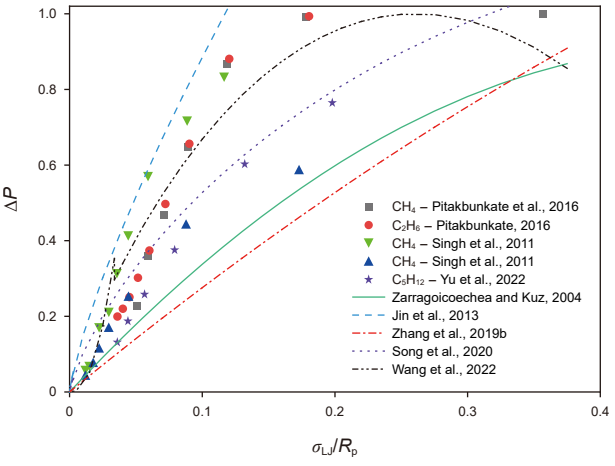

Fig. 6. Comparison of critical pressure shift calculated from different models with the data points.

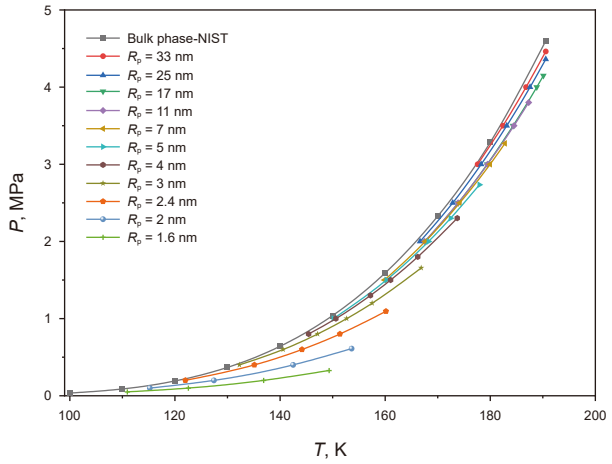

Fig. 7. *P-T* phase diagram of methane in nanopores with different radii (National Institute of Standards and Technology (NIST)).

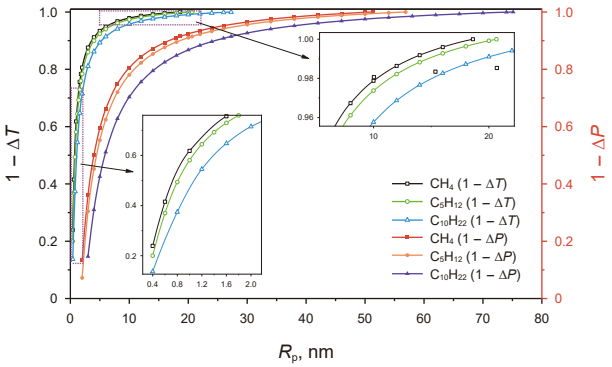

Fig. 8. Critical properties shift of confined methane, pentane and decane calculated by m-PR EOS.

when $R_p > 18.62$ nm, the critical temperature of methane no longer shifts, and when $R_p > 51.33$ nm, the critical pressure of methane no longer shifts. The critical pore sizes for pentane and decane are also shown in Fig. 8. Given a fixed contact angle, the critical property shifts for other hydrocarbons can also be calculated using the same method to elucidate the influence of pore size.

3.3. Bubble point calculation of binary hydrocarbon fluids and comparison

The data used for fitting and validation was extracted from various research methods, which involve different surface compositions, wettability, and research approaches, and the m-PR EOS calculation results in this study are influenced to some extent by the pure hydrocarbon data provided by numerous scholars. To ensure the applicability of the m-PR EOS, a comparison is also made with the results of binary hydrocarbon studies from other scholars. As shown in Table 3, the critical property data for the binary mixtures were obtained from simulations with two different wall materials. Specifically, the first six simulations employed silica walls (Cho et al., 2017), whereas the latter six used graphite layers (Pitakbunkate et al., 2016). To ensure the validation procedure closely matches that of the referenced studies, the contact angle was set to $\theta = 30°$ (Xu et al., 2018) for the first six validation cases and $\theta = 60°$ (Wu et al., 2016) for the latter six. The comparative results indicate that the theoretical model and updated mixing rules proposed in this study

Table 3
Measured and calculated bubble-point pressures for the CH_4-$C_{10}H_{22}$, and CH_4-C_8H_{18} (Cho et al., 2017) and CH_4-C_2H_6 (Pitakbunkate et al., 2016) mixtures at different temperatures and pore radii.

System, mol%	T, K	R_p, nm	$P_{b\text{-}BP}$[a], kPa	$P_{b\text{-}BP}$[b], kPa	Change[c], %	$P_{b\text{-}BP}$[d], kPa	Change[e], %	AD[f], %
10.00 C_1-90.00 C_{10}	311.15	3.5	2579	1669	35.28	1858	27.97	11.30
		3.7	2579	2034	21.13	1906	26.08	6.28
10.00 C_1-90.00 C_{10}	325.15	3.5	2717	2220	18.29	207	23.77	6.70
		3.7	2717	2468	9.16	2128	21.67	13.77
10.00 C_1-90.00 C_8	311.15	3.5	2503	1765	29.48	1881	24.85	6.57
		3.7	2503	2186	12.66	1977	21.03	9.57
30.02 C_1-69.98 C_2	250.15	5	4311	3818	11.45	3747	13.07	1.85
	233.15	5	3284	2999	8.68	2894	11.87	3.49
	220.15	5	2589	2392	7.61	2296	11.33	4.03
50.00 C_1-50.00 C_2	230	5	4768	4173	12.48	4150	12.95	0.54
	220.15	5	4028	3645	9.51	3499	13.12	4.00
	210.15	5	3327	3118	6.28	2907	12.62	6.77

Notes:
[a] Measured bubble-point pressure in bulk phase.
[b] Measured bubble-point pressure at the pore radius R_p.
[c] Change of the measured bubble-point pressure in bulk phase and porous medium in percentage.
[d] Bubble-point pressure calculated in this study at the pore radius R_p.
[e] Change between the measured bubble-point pressure in bulk phase and the bubble-point pressure calculated in this study at the pore radius of R_p in percentage.
[f] Absolute deviation between the measured bubble-point pressure at the pore radius of R_p and the bubble-point pressure calculated in this study at the pore radius of R_p.

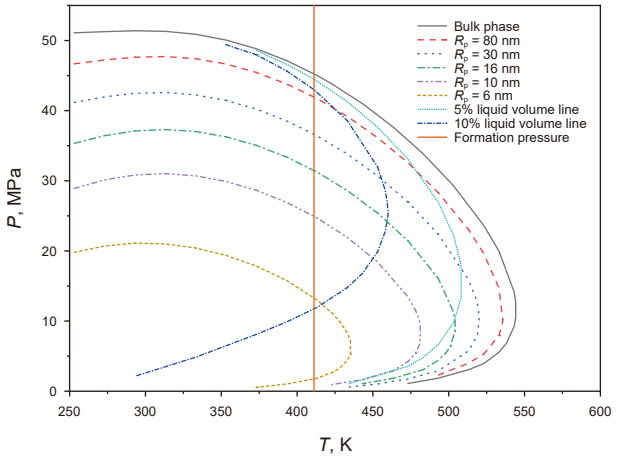

Fig. 9. *P-T* phase diagram of mixture hydrocarbons in nanopores with different radii.

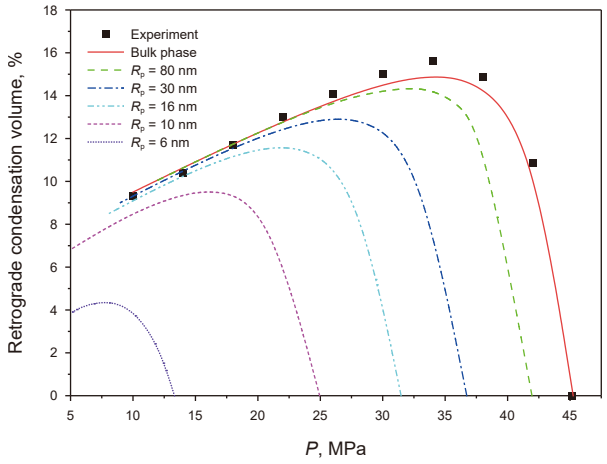

Fig. 10. Impact of pressure decline on retrograde condensation volume of mixture hydrocarbons in nanopores with different radii.

yield calculations for the critical property shifts of multi-component hydrocarbon fluids in nanoporous spaces that closely match the relevant experimental data. This model is capable of reliably predicting the phase behavior of multi-component hydrocarbon fluids in the nanopores of shale reservoirs.

3.4. Phase diagram prediction for shale gas condensate samples and the CCE experiment

Furthermore, this study used the developed m-PR EOS to predict the phase diagram of the recombined shale gas condensate sample (the reservoir temperature is 411.15 K and the reservoir pressure is 61.2 MPa) and conducted a CCE test. Initially, this study divided the composition of the recombined shale gas condensate sample into five pseudo-components and fit the CCE and bubble point experimental data. The m-PR EOS proposed in this study calculates the phase diagrams and quality lines for the fluid in both bulk phase and nanopores with different radii (6–80 nm), as shown in Fig. 9. The results indicate that as pore size decreases, the overall envelope of the phase diagram shrinks towards the lower-left, and the shrinkage rate increases with smaller pore sizes, which aligns with the observations for critical temperature and critical pressure. The quality lines near the critical point region are densely packed, meaning that even small changes in temperature and pressure can induce significant variations in the distribution of gas and liquid phases. In the current study, only an approximate range for the critical point can be calculated through the program (with the critical pressure around 51 MPa and critical temperature around 320 K), and thus it is not explicitly marked in Fig. 9. Meanwhile, this study carried out a sensitivity analysis using Python code with numerical precision set to 10^{-6}. The analysis found that near the critical point, a temperature change of only 0.1 K can produce up to a 4.95% change in liquid saturation, while a pressure change of 0.1 MPa can produce up to a 13.76% change in liquid saturation.

Fig. 9 also shows the phase envelope and quality lines for different pore sizes intersected by the formation temperature line. This allows for accurately determining the dew point pressure and retrograde condensation behavior in various pore sizes. The quality lines can precisely predict the distribution of the gas-liquid phases.

As shown in Fig. 10, the m-PR EOS proposed in this study can predict the variation trends of both dew point pressure and condensate oil saturation in different pore spaces. By combining the prediction results with the critical flow saturation parameters

of the gas-liquid phase, it is possible to determine the specific nanopore scales from which the produced oil and gas originate under different production pressures, thus fully understanding the dynamic characteristics of oil and gas migration in nanopores. Therefore, the m-PR EOS proposed in this study can provide important production guidance for condensate oil extraction and oilfield development.

As shown in Fig. 11, the smaller the pore size, the lower the dew point pressure of shale condensate gas. As the pore size increases, its dew point pressure gradually increases, with the rate of increase slowing down and approaching that of the bulk phase. The conclusion is in line with the current consensus among scholars on nano-confinement effects in this field.

Fig. 12 illustrates the influence of the contact angle between mixed hydrocarbon fluids and the pore wall on the *P-T* phase diagram when $R_p = 16$ nm. According to the expression for capillary pressure, a smaller contact angle corresponds to stronger capillary pressure within the pores, leading to more pronounced anomalous intermolecular interactions. Consequently, the critical property shifts of hydrocarbon fluids in nanopores become more significant, and the phase diagram shifts further toward the lower-left direction. Additionally, the results show that the phase diagram at $\theta = 120°$ coincides with that of the bulk phase, which is consistent with the findings of Feng et al. (2021). This indicates that as the

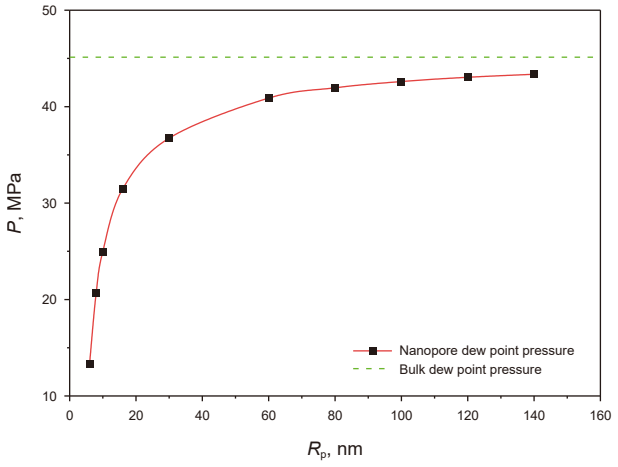

Fig. 11. The variation of the dew point of shale condensate gas with pore radius.

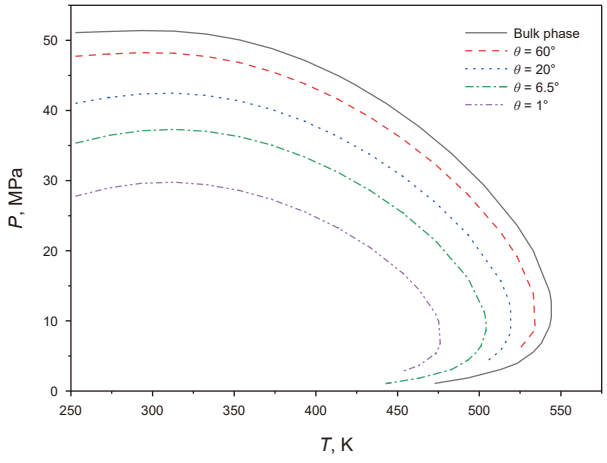

Fig. 12. *P-T* phase diagram of mixture hydrocarbons in nanopores with different contact angles.

contact angle increases, the influence of capillary pressure on the critical property shifts of confined hydrocarbons decreases.

In summary, this study establishes a thermodynamic framework that clearly quantifies how the coupling of pore size and wettability alters the phase behavior of both pure hydrocarbon fluids and complex hydrocarbon mixtures, and accurately predicts the resulting changes in their phase envelopes and CCE. The model is capable of predicting nanoscale hydrocarbon phase behavior with unprecedented accuracy, especially in complex shale systems characterized by heterogeneous wettability. Compared to previously modified equations of state (Cui et al., 2018; Jin and Nasrabadi, 2016; Song et al., 2020; Wang et al., 2022; Zhang et al., 2019b), none of them have fully accounted for the combined effects of wettability, adsorption, and pore size on hydrocarbon phase behavior—those EOSs have typically performed well only when applied to specific oilfield regions. By introducing variations in the contact angle between the rock surface and the fluid, our work extends the applicability of the modified EOS to all oilfield blocks, enabling seamless integration into numerical simulation software and broad application in shale oil and gas production, thereby significantly enhancing its impact and industrial value (Dong et al., 2016; Li and Sheng, 2017). The model's ability to accurately predict shifts in the critical properties of shale oil and gas can be directly applied to reservoirs with diverse characteristics, making an important contribution to preventing retrograde condensation damage (Liu and Zhang, 2019). Furthermore, its prediction of the critical pore size precisely distinguishes bulk phase fluids from confined phase fluids—a capability that is crucial for optimizing extraction strategies in shale condensate gas reservoirs, where nanoscale confinement profoundly influences production dynamics. The m-PR EOS proposed here synthesizes and integrates numerous microscopic findings, such as those from molecular simulations (Jin and Nasrabadi, 2016; Li et al., 2014; Morishige et al., 1997; Pitakbunkate et al., 2016; Singh and Singh, 2011; Singh et al., 2009; Vishnyakov and Neimark, 2009; Vishnyakov et al., 2001; Yu et al., 2022; Zarragoicoechea and Kuz, 2002), into a comprehensive methodology for oilfield application (Dong et al., 2016; Li and Sheng, 2017), accurately forecasting micro- and nanopore phase behavior in shale and serving as a vital bridge between microscopic mechanism research and macroscopic field production strategies.

In future work, we will use molecular simulation to conduct a more in-depth mechanistic analysis of the distribution and transport of complex hydrocarbon mixtures in nanoscale pores, integrate the resulting findings into the equation of state, and improve its accuracy for field-scale predictions. We expect the follow-up research to serve as a bridge between microscopic mechanistic analysis and macroscopic field-scale applications.

4. Conclusions

(1) A novel physical model for the modified EOS is formulated, leading to the development of a new m-PR EOS by concurrently integrating the adsorption interactions between wall-fluid molecules in nanopores and the anomalous intermolecular interactions between fluid molecules.
(2) Two new analytical expressions are derived and fitted to describe the degree of critical property shifts for fluids under different nanopore sizes. Validation through data analysis and comparison with results from other studies confirms the reliability of the m-PR EOS in predicting the critical properties of both pure and binary hydrocarbon fluids.
(3) This work pioneers the integration of critical pore size determination into the PR EOS framework. *P-T* phase

diagrams for pure hydrocarbon fluids in nanopores of varying sizes are presented. The results indicate that when the pore size is smaller than the critical pore size, both the critical temperature and pressure decrease with decreasing pore size, and the rate of decrease accelerates accordingly.

(4) The comparative analysis of the critical property shifts for methane, pentane, and decane shows that, at the same pore size, the degree of shift in the critical properties increases with increasing Lennard-Jones molecular size parameter σ_{LJ}.

(5) The m-PR EOS was used to compute *P-T* phase diagrams and CCE data for fluids in a shale condensate gas reservoir across different pore sizes and contact angles. As pore size decreases, both the *P-T* diagrams and condensate saturation curves contract toward the lower-left—resulting in lower dew point pressures and maximum retrograde oil saturations; and smaller contact angles further amplify the shifts in critical properties.

CRediT authorship contribution statement

Hong-Xian Kuang: Writing – review & editing, Writing – original draft, Visualization, Validation, Software, Methodology, Investigation, Formal analysis, Data curation, Conceptualization. **Zhou-Hua Wang:** Writing – review & editing, Supervision, Resources, Project administration, Methodology, Investigation, Funding acquisition, Data curation, Conceptualization. **Na Jia:** Writing – review & editing, Validation, Supervision, Methodology, Investigation, Formal analysis. **Han-Min Tu:** Supervision, Project administration, Methodology, Investigation. **Yun Li:** Writing – review & editing, Methodology, Investigation. **Huang Liu:** Resources, Investigation. **Ping Guo:** Supervision, Methodology. **Zi-Yan Wang:** Investigation.

Declaration of competing Interest

The authors declare that they have no known competing financial interests or personal relationships that could have appeared to influence the work reported in this paper.

Acknowledgments

This work was supported by National Natural Science Foundation of China (52074236, 42402037).

Nomenclature

a	Attraction parameter in the PR EOS
a'	Attraction parameter in the modified PR EOS
b	Co-volume parameter in the PR EOSs
α	Temperature-dependent parameter
C	Attractive modified parameter
θ	Contact angle
V_m	Molar volume calculated by the original PR EOS, m^3/kmol
V'_m	Molar volume calculated by the modified PR EOS, m^3/kmol
P	Pressure, MPa
P_c	Critical pressure of the original PR EOS, MPa
P_{cm}	Critical pressure of the modified PR EOS, MPa
T	Temperature, K
T_r	Reduced temperature
T_c	Critical temperature of the original PR EOS, K
T_{cm}	Critical temperature of the modified PR EOS, K
V	Volume
R	Ideal gas constant
ΔP_c	Shift of critical pressure
ΔT_c	Shift of critical temperature
n_t	Total number of fluid molecules
n_f	Number of free fluid molecules
n_a	Number of adsorbed fluid molecules
ρ_t	Density of fluid molecules
ρ_f	Density of free fluid molecules
ρ_a	Density of adsorbed fluid molecules
R_p	Pore radius, nm
δ_{ij}	Binary interaction coefficient
ω	Acentric factor
σ_{LJ}	The Lennard-Jones molecular size parameter
μ	Percentage of adsorbed molecules relative to the total number of molecules in the nanopore
ξ	Reduced adsorption density
m and n	Correlated parameters of adsorption layer thickness
M	Molecular weight
φ_i^V and φ_i^L	Fugacity coefficients of component i in the vapor and liquid phases
Z_V and Z_L	Compressibility factors of the vapor and liquid phases

Appendix A

This section presents the derivation of the parameters a and b in the m-PR EOS, along with the formulation of the fugacity coefficient expression for vapor-liquid equilibrium calculations. Subsequently, updated mixing rules are introduced to predict the critical properties of the multi-component hydrocarbon fluids.

The refinement procedure for the m-PR EOS is outlined as follows:

$$P = \frac{RT}{V'_m - b} - \frac{\alpha a'}{V'_m(V'_m + b) + b(V'_m - b)} \tag{A.1}$$

where

$$V'_m = \frac{V_m}{1 + \mu\xi} \tag{A.2}$$

$$\mu = 1 - \frac{\rho_f (R_p - \delta)^2}{\rho_t R_p^2} \tag{A.3}$$

$$\xi = \frac{\rho_f}{\rho_a} - 1 \tag{A.4}$$

$$a' = a \times \left(1 - C \ln\left(\frac{180}{\theta}\right)\frac{\sigma_{LJ}}{R_p}\right) \tag{A.5}$$

Applying the critical point restrictions to Eq. (A.1):

$$\left(\frac{\partial P}{\partial V}\right)_{T=T_c} = -\frac{RT_c/(1+\mu\xi)}{(V_c/(1+\mu\xi)-b)^2} + \frac{2a'(V_c/(1+\mu\xi)+b)/(1+\mu\xi)}{[V_c/(1+\mu\xi)(V_c/(1+\mu\xi)+b)+b(V_c/(1+\mu\xi)-b)]^2} = 0 \tag{A.6}$$

$$\left(\frac{\partial^2 P}{\partial V^2}\right)_{T=T_c} = \frac{2RT_c\Big/(1+\mu\xi)^2}{(V_c/(1+\mu\xi)-b)^3} + \frac{2a'[b(V_c/(1+\mu\xi)-b)-(V_c/(1+\mu\xi)+b)(3V_c/(1+\mu\xi)+4b)]\Big/(1+\mu\xi)^2}{[V_c/(1+\mu\xi)(V_c/(1+\mu\xi)+b)+b(V_c/(1+\mu\xi)-b)]^3} = 0 \tag{A.7}$$

From Eq. (A.6), it is represented as

$$\frac{RT_c}{(V_c/(1+\mu\xi)-b)^3} + \frac{2a'(V_c/(1+\mu\xi)+b)}{[V_c/(1+\mu\xi)(V_c/(1+\mu\xi)+b)+b(V_c/(1+\mu\xi)-b)]^2(V_c/(1+\mu\xi)-b)} = 0 \tag{A.8}$$

Imposing Eq. (A.8) on Eq. (A.7), it is given as

$$\frac{2(V_c/(1+\mu\xi)+b)}{V_c/(1+\mu\xi)-b} = \frac{(V_c/(1+\mu\xi)+b)(3V_c/(1+\mu\xi)+4b)-b(V_c/(1+\mu\xi)-b)}{(V_c/(1+\mu\xi))(V_c/(1+\mu\xi)+b)+b(V_c/(1+\mu\xi)-b)} \tag{A.9}$$

It can be rewritten as

$$-(V_c/(1+\mu\xi)+b)(V_c/(1+\mu\xi)-b)(3V_c/(1+\mu\xi)+2b)+2(V_c/(1+\mu\xi))(V_c/(1+\mu\xi)+b)^2+b(V_c/(1+\mu\xi)-b)^2 = 0 \tag{A.10}$$

Assuming $b = kV_c/(1+\mu\xi)$, Eq. (A.10) can be rewritten as

$$3k^3+3k^2+3k-1=0 \tag{A.11}$$

By solving Eq. (A.11), it can be rewritten as

$$b = \frac{0.25308V_c}{(1+\mu\xi)} \tag{A.12}$$

By imposing Eq. (A.12) into Eq. (A.6),

$$-\frac{RT_c}{(1-k)^2} + \frac{2a'(1+k)}{(V_c/(1+\mu\xi))[(1+k)+k(1-k)]^2} = 0 \tag{A.13}$$

The parameters a are rearranged to give

$$a' = \frac{RT_c(V_c/(1+\mu\xi))[(1+k)+k(1-k)]^2}{2a(1+k)(1-k)^2} = 1.48742\frac{RT_cV_c}{(1+\mu\xi)} \tag{A.14}$$

$$\frac{P_cV_c}{RT_c} = 0.30740(1+\mu\xi) \tag{A.15}$$

In the traditional PR-EOS, it is given as

$$b = 0.25308V_c \tag{A.16}$$

From Eqs. (A.14–A.16), the parameters a and b are given:

$$a = 0.45724\frac{R^2T_c^2}{P_c\left(1-C\ln\left(\frac{180}{\theta}\right)\frac{\sigma_{LJ}}{R_p}\right)} \tag{A.17}$$

$$b = 0.07780\frac{RT_c}{P_c}(1+\mu\xi) \tag{A.18}$$

Imposing m-PR EOS into the compressibility factor form gives

$$Z^3-(1-B)Z^2+\left(A-3B^2-2B\right)Z-\left(AB-B^2-B^3\right)=0 \quad (A.19)$$

with

$$A_V=\frac{\alpha a' P^V}{(RT)^2}=\frac{\left[\alpha a\times\left(1-C\frac{\sigma_{LJ}}{R_p}\right)\right]P^V}{(RT)^2},\ B_V=\frac{bP^V}{RT}(1+\mu\xi)=\frac{bP^V(1-\Delta T_c)}{RT\left(1-C\frac{\sigma_{LJ}}{R_p}\right)} \quad (A.20)$$

$$A_L=\frac{\alpha a' P^L}{(RT)^2}=\frac{\left[\alpha a\times\left(1-C\frac{\sigma_{LJ}}{R_p}\right)\right]P^L}{(RT)^2},\ B_L=\frac{bP^L}{RT}(1+\mu\xi)=\frac{bP^L(1-\Delta T_c)}{RT\left(1-C\frac{\sigma_{LJ}}{R_p}\right)} \quad (A.21)$$

where

$$(\alpha a')_m=\sum_i\sum_j x_i x_j\left(a_i' a_j'\right)^{0.5}\left(1-\delta_{ij}\right) \quad (A.22)$$

$$(\alpha a')_m=\sum_i\sum_j x_i x_j\left(\left(a_i\times\left(1-C\frac{\sigma_{LJ}}{R_p}\right)\right)\left(a_j\times\left(1-C\frac{\sigma_{LJ}}{R_p}\right)\right)\right)^{0.5}\left(1-\delta_{ij}\right) \quad (A.23)$$

$$b_m=\sum_{i=1}^{n}x_i b \quad (A.24)$$

For the pure hydrocarbon fluids, the fugacity coefficient is expressed as follows:

$$\ln\varphi_{pure}=-\ln[Z-B]+(Z-1)+\frac{A}{2\sqrt{2}B}\ln\left[\frac{Z+B\left(1+\sqrt{2}\right)}{Z+B\left(1-\sqrt{2}\right)}\right] \quad (A.25)$$

For a mixture,

$$\ln\varphi_i^V=-\ln[Z_V-B_V]+\frac{b_i}{b}(Z_V-1)+\frac{A_V}{2\sqrt{2}B_V}\left[\frac{1}{a'}\left(2\sqrt{a_i'}\sum_{j=1}^{nc}z_j\sqrt{a_i'}\left(1-\delta_{ij}\right)\right)-\frac{b_i}{b}\right]\ln\left[\frac{Z_V+B_V\left(1+\sqrt{2}\right)}{Z_V+B_V\left(1-\sqrt{2}\right)}\right] \quad (A.26)$$

$$\ln\varphi_i^L=-\ln[Z_L-B_L]+\frac{b_i}{b}(Z_L-1)+\frac{A_L}{2\sqrt{2}B_L}\left[\frac{1}{a'}\left(2\sqrt{a_i'}\sum_{j=1}^{nc}z_j\sqrt{a_i'}\left(1-\delta_{ij}\right)\right)-\frac{b_i}{b}\right]\ln\left[\frac{Z_L+B_L\left(1+\sqrt{2}\right)}{Z_L+B_L\left(1-\sqrt{2}\right)}\right] \quad (A.27)$$

References

Alfi, M., Nasrabadi, H., Banerjee, D., 2016. Experimental investigation of confinement effect on phase behavior of hexane, heptane and octane using lab-on-a-chip technology. Fluid Phase Equilib. 423, 25–33. https://doi.org/10.1016/j.fluid.2016.04.017.

Arif, M., Lebedev, M., Barifcani, A., et al., 2017. Influence of shale-total organic content on CO_2 geo-storage potential. Geophys. Res. Lett. 44 (17), 8769–8775. https://doi.org/10.1002/2017GL073532.

Arif, M., Zhang, Y., Iglauer, S., 2021. Shale wettability: Data sets, challenges, and outlook. Energy Fuel. 35 (4), 2965–2980. https://doi.org/10.1021/acs.energyfuels.0c04120.

Bhutto, D.K., Shar, A.M., Abbasi, G.R., et al., 2022. Shale wettability characteristics via air/brines and air/oil contact angles and influence of controlling factors: A case study of lower Indus Basin, Pakistan. ACS Omega 8 (1), 688–701. https://doi.org/10.1021/acsomega.2c05960.

Caineng, Z., Rukai, Z., Zhongqiang, C., et al., 2019. Organic-matter-rich shales of China. Earth Sci. Rev. 189, 51–78. https://doi.org/10.1016/j.earscirev.2018.12.002.

Cho, H., Bartl, M.H., Deo, M., 2017. Bubble point measurements of hydrocarbon mixtures in mesoporous media. Energy Fuel. 31 (4), 3436–3444. https://doi.org/10.1021/acs.energyfuels.6b02424.

Cui, X., Yang, E., Song, K., et al., 2018. Phase equilibrium of hydrocarbons confined in nanopores from a modified Peng-Robinson Equation of State. In: The SPE Annual Technical Conference and Exhibition. Dallas.

Dong, X., Liu, H., Hou, J., et al., 2016. Phase equilibria of confined fluids in nanopores of tight and shale rocks considering the effect of capillary pressure and adsorption film. Ind. Eng. Chem. Res. 55 (3), 798–811. https://doi.org/10.1021/acs.iecr.5b04276.

Dong, X., Xu, W., Liu, R., et al., 2022. Insights into adsorption and diffusion behavior of shale oil in slit nanopores: a molecular dynamics simulation study. J. Mol. Liq. 359, 119322. https://doi.org/10.1016/j.molliq.2022.119322.

Dubinin, M.M., 1960. The potential theory of adsorption of gases and vapors for adsorbents with energetically nonuniform surfaces. Chem. Rev. (2), 235–241. https://doi.org/10.1021/cr60204a006.

Feng, D., Bakhshian, S., Wu, K., et al., 2021. Wettability effects on phase behavior and interfacial tension in shale nanopores. Fuel 290, 119983. https://doi.org/10.1016/j.fuel.2020.119983.

Foo, K.Y., Hameed, B.H., 2010. Insights into the modeling of adsorption isotherm systems. Chem. Eng. J. 1, 2–10. https://doi.org/10.1016/j.cej.2009.09.013.

Fu, J., Hao, Y., Su, Y., et al., 2023. Critical properties and phase behavior of confined fluids in irregular nanopores of shale gas reservoir. Gas Sci. Eng. 116, 205002. https://doi.org/10.1016/j.jgsce.2023.205002.

Jang, Y., Chung, E., 2019. Influence of alkanes on lithium adsorption and desorption of a H_2TiO_3 ion sieve adsorbent in synthetic shale gas-produced water. Ind. Eng. Chem. Res. 58 (48), 21897–21903. https://doi.org/10.1021/acs.iecr.9b04472.

Jia, C., Zheng, M., Zhang, Y., 2012. Unconventional hydrocarbon resources in China and the prospect of exploration and development. Petrol. Explor. Dev. (2), 139–146. https://doi.org/10.1016/S1876-3804(12)60026-3.

Jiang, J., Sandler, S.I., Smit, B., 2004. Capillary phase transitions of n-alkanes in a carbon nanotube. Nano Lett. 4 (2), 241–244. https://doi.org/10.1021/nl034961y.

Jin, B., Nasrabadi, H., 2016. Phase behavior of multi-component hydrocarbon systems in nano-pores using gauge-GCMC molecular simulation. Fluid Phase Equilib. 425, 324–334. https://doi.org/10.1016/j.fluid.2016.06.018.

Jin, L., Ma, Y., Jamili, A., 2013. Investigating the effect of pore proximity on phase behavior and fluid properties in shale formations. In: The SPE Annual Technical Conference and Exhibition. New Orleans.

Kuila, U., Prasad, M., 2013. Specific surface area and pore-size distribution in clays and shales. Geophys. Prospect. 61 (2), 341–362. https://doi.org/10.1111/1365-2478.12028.

Li, L., Sheng, J.J., 2017. Nanopore confinement effects on phase behavior and capillary pressure in a Wolfcamp shale reservoir. J. Taiwan Inst. Chem. Eng. 78 (C), 317–328. https://doi.org/10.1016/j.jtice.2017.06.024.

Li, Z., Jin, Z., Firoozabadi, A., 2014. Phase behavior and adsorption of pure substances and mixtures and characterization in nanopore structures by density functional theory. SPE J. 19 (6), 109. https://doi.org/10.2118/169819-pa.

Liu, X., Zhang, D., 2019. A review of phase behavior simulation of hydrocarbons in confined space: implications for shale oil and shale gas. J. Nat. Gas Sci. Eng. 68 (0), 102901. https://doi.org/10.1016/j.jngse.2019.102901.

Liu, Y., Zong, P., Wang, L., et al., 2024. Quantitative characterization of inorganic pores in Sinian Doushantou Dolomitic Shale based on FIB-SEM in Western Hubei Province, China. ACS Omega 9 (7), 8151–8161. https://doi.org/10.1021/acsomega.3c08640.

Luo, S., Lutkenhaus, J.L., Nasrabadi, H., 2018. Use of differential scanning calorimetry to study phase behavior of hydrocarbon mixtures in nano-scale porous media. J. Petrol. Sci. Eng. 163, 731–738. https://doi.org/10.1016/j.petrol.2016.12.019.

Luo, S., Nasrabadi, H., Lutkenhaus, J.L., 2016. Effect of confinement on the bubble points of hydrocarbons in nanoporous media. AIChE J. 62 (5), 1772–1780. https://doi.org/10.1002/aic.15154.

Ma, Y., Jamili, A., 2016. Modeling the density profiles and adsorption of pure and mixture hydrocarbons in shales. J Unconventional Oil Gas Resources 14, 128–138. https://doi.org/10.1016/j.juogr.2016.03.003.

Milad, M., Junin, R., Sidek, A., et al., 2021. Huff-n-Puff Technology for enhanced oil recovery in shale/tight oil reservoirs: progress, gaps, and perspectives. Energy Fuel. 35 (21), 17279–17333. https://doi.org/10.1021/acs.energyfuels.1c02561.

Morishige, K., Fujii, H., Uga, M., et al., 1997. Capillary critical point of argon, nitrogen, oxygen, ethylene, and carbon dioxide in MCM-41. Langmuir 13 (13), 3494–3498. https://doi.org/10.1021/la970079u.

Mota, J.P.B., Esteves, I.A.A.C., 2007. Simplified gauge-cell method and its application to the study of capillary phase transition of propane in carbon nanotubes. Adsorption: J. Int. Adsorpt. Soc. 13 (1), 21–32. https://doi.org/10.1007/s10450-007-9006-8.

Pan, B., Li, Y., Wang, H., et al., 2018. CO_2 and CH_4 wettabilities of organic-rich shale. Energy Fuel. 32 (2), 1914–1922. https://doi.org/10.1021/acs.energyfuels.7b01147.

Pang, W., He, Y., Yan, C., et al., 2019. Tackling the challenges in the estimation of methane absolute adsorption in kerogen nanoporous media from molecular and analytical approaches. Fuel 242, 687–698. https://doi.org/10.1016/j.fuel.2019.01.059.

Parsa, E., Yin, X., Ozkan, E., 2015. In: Direct Observation of the Impact of Nanopore Confinement on Petroleum Gas Condensation. Paper Presented at the SPE Annual Technical Conference and Exhibition.

Peng, D., Robinson, D.B., 1976. A new two-constant equation of state. Ind. Eng. Chem. Fundam. 15 (1), 59–64. https://doi.org/10.1021/i160057a011.

Pitakbunkate, T., Balbuena, P.B., Moridis, G.J., et al., 2016. Effect of confinement on pressure/volume/temperature properties of hydrocarbons in shale reservoirs. SPE J. 21 (2), 621–634. https://doi.org/10.2118/170685-pa.

Qiu, X., Tan, S.P., Dejam, M., et al., 2018. Simple and accurate isochoric differential scanning calorimetry measurements: phase transitions for pure fluids and mixtures in nanopores. Phys. Chem. Chem. Phys. 21 (1), 224–231. https://doi.org/10.1039/c8cp06691d.

Russo, P.A., Ribeiro Carrott, M.M.L., Carrott, P.J.M., 2012. Trends in the condensation/evaporation and adsorption enthalpies of volatile organic compounds on mesoporous silica materials. Microporous Mesoporous Mater. 151 (1), 223–230. https://doi.org/10.1016/j.micromeso.2011.10.032.

Santos, M.S., Franco, L.F.M., Castier, M., et al., 2018. Molecular dynamics simulation of n-alkanes and CO_2 confined by calcite nanopores. Energy Fuel. 32 (2), 1934–1941. https://doi.org/10.1021/acs.energyfuels.7b02451.

Singh, S.K., Singh, J.K., 2011. Effect of pore morphology on vapor–liquid phase transition and crossover behavior of critical properties from 3D to 2D. Fluid Phase Equilib. 300 (1), 182–187. https://doi.org/10.1016/j.fluid.2010.10.014.

Singh, S.K., Sinha, A., Deo, G., et al., 2009. Vapor-liquid phase coexistence, critical properties, and surface tension of confined alkanes. J. Phys. Chem. C 113 (17), 7170–7180. https://doi.org/10.1021/jp8073915.

Song, Z., Song, Y., Guo, J., et al., 2020. Adsorption induced critical shifts of confined fluids in shale nanopores. Chem. Eng. J. 385, 123837. https://doi.org/10.1016/j.cej.2019.123837.

Tan, S.P., Qiu, X., Dejam, M., et al., 2019. Critical point of fluid confined in nanopores: experimental detection and measurement. J. Phys. Chem. C 123 (15), 9824–9830. https://doi.org/10.1021/acs.jpcc.9b00299.

Tian, S.S., Erastova, V., Lu, S.F., et al., 2018. Understanding model crude oil component interactions on kaolinite silicate and aluminol surfaces: toward improved understanding of shale oil recovery. Energy Fuel. 32 (2), 1155–1165. https://doi.org/10.1021/acs.energyfuels.7b02763.

Tian, Y., Yan, C., Jin, Z., 2017. Characterization of methane excess and absolute adsorption in various clay nanopores from molecular simulation. Sci. Rep. 7 (1), 12040. https://doi.org/10.1038/s41598-017-12123-x.

Vishnyakov, A., Neimark, A.V., 2009. Multicomponent gauge cell method. J. Chem. Phys. 130 (22), 224103. https://doi.org/10.1063/1.3124186.

Vishnyakov, A., Piotrovskaya, E.M., Brodskaya, E.N., et al., 2001. Critical properties of Lennard-Jones fluids in narrow slit-shaped pores. Langmuir 17 (14), 4451–4458. https://doi.org/10.1021/la001641a.

Wang, L., Parsa, E., Gao, Y., et al., 2014. Experimental study and modeling of the effect of nanoconfinement on hydrocarbon phase behavior in unconventional reservoirs. In: The SPE Western Regional Meeting. Denver.

Wang, P., Huang, S., Zhao, F., et al., 2022. Modeling phase behavior of nano-confined fluids in shale reservoirs with a modified Soave-Redlich-Kwong equation of state. Chem. Eng. J. 433, 133661. https://doi.org/10.1016/j.cej.2021.133661.

Wang, S., Feng, Q.H., Zha, M., et al., 2015. Molecular dynamics simulation of liquid alkane occurrence state in pores and slits of shale organic matter. Petrol. Explor. Dev. 42 (6), 844–851. https://doi.org/10.1016/s1876-3804(15)30081-1.

Wang, S., Feng, Q., Javadpour, F., et al., 2015. Oil adsorption in shale nanopores and its effect on recoverable oil-in-place. Int. J. Coal Geol. 147–148, 9–24. https://doi.org/10.1016/j.coal.2015.06.002.

Wang, S., Feng, Q., Zha, M., et al., 2015. Molecular dynamics simulation of liquid alkane occurrence state in pores and slits of shale organic matter. Petrol. Explor. Dev. 42 (6), 844–851. https://doi.org/10.1016/S1876-3804(15)30081-1.

Wang, X., Zhang, K., Jiang, Z., et al., 2025. Hydrocarbon generation and pore evolution in marine organic-rich shales across maturation stages. Fuel 402, 136050. https://doi.org/10.1016/j.fuel.2025.136050.

Wang, Z., Yu, C., Zhao, J., et al., 2025. The phase transition characteristics of n-pentane in silica slits with different wettability by Monte Carlo method. Sci. Rep. 15 (1), 7332. https://doi.org/10.1038/s41598-025-89207-6.

Wu, C., Li, Y., Woon, W., et al., 2016. Contact angle hysteresis on graphene surfaces and hysteresis-free behavior on oil-infused graphite surfaces. Appl. Surf. Sci. 385, 153–161. https://doi.org/10.1016/j.apsusc.2016.05.059.

Wu, Y., Cheng, L., Ma, L., et al., 2021. A transient two-phase flow model for production prediction of tight gas wells with fracturing fluid-induced formation damage. J. Petrol. Sci. Eng. 199, 108351. https://doi.org/10.1016/j.petrol.2021.108351.

Xing, X., Feng, Q., Zhang, W., et al., 2021. Vapor-liquid equilibrium and criticality of CO_2 and n-heptane in shale organic pores by the Monte Carlo simulation. Fuel 299, 120909. https://doi.org/10.1016/j.fuel.2021.120909.

Xu, S., Wang, J., Wu, J., et al., 2018. Oil contact angles in a water-decane-silicon dioxide system: effects of surface charge. Nanoscale Res. Lett. 13 (1). https://doi.org/10.1186/s11671-018-2521-6.

Xu, Y., Lun, Z., Pan, Z., et al., 2022. Occurrence space and state of shale oil: A review. J. Pet. Sci. Eng. 211, 110183. https://doi.org/10.1016/j.petrol.2022.110183.

Yang, G., Fan, Z., Li, X., 2019. Determination of confined fluid phase behavior using extended Peng-Robinson equation of state. Chem. Eng. J. 378, 122032. https://doi.org/10.1016/j.cej.2019.122032.

Yu, C., Zhao, J., Wang, Z., et al., 2022. Vapor-liquid phase equilibrium of n-pentane in quartz nanopores by grand canonical Monte Carlo calculation. J. Mol. Liq. 365, 120075. https://doi.org/10.1016/j.molliq.2022.120075.

Yu, Y.X., Gao, G.H., 2000. Lennard-Jones chain model for self-diffusion of n-Alkanes. Int. J. Thermophys. 21 (1), 57–70. https://doi.org/10.1023/A:1006652703917.

Yun, J., Düren, T., Keil, F.J., et al., 2002. Adsorption of methane, ethane, and their binary mixtures on MCM-41: Experimental evaluation of methods for the prediction of adsorption equilibrium. Langmuir 18 (7), 2693–2701. https://doi.org/10.1021/la0155855.

Zarragoicoechea, G.J., Kuz, V.A., 2002. van der Waals equation of state for a fluid in a nanopore. Phys. Rev. E: Stat., Nonlinear, Soft Matter Phys. 65 (2), 21110. https://doi.org/10.1103/PhysRevE.65.021110.

Zarragoicoechea, G.J., Kuz, V.A., 2004. Critical shift of a confined fluid in a nanopore. Fluid Phase Equilib. 220 (1), 7–9. https://doi.org/10.1016/j.fluid.2004.02.014.

Zeigermann, P., Dvoyashkin, M., Valiullin, R., et al., 2009. Assessing the pore critical point of the confined fluid by diffusion measurement. Diffus. Fundament. https://doi.org/10.62721/diffusion-fundamentals.11.493.

Zhang, K., Jia, N., Liu, L., 2018. Adsorption thicknesses of confined pure and mixing fluids in nanopores. Langmuir 34 (43), 12815–12826. https://doi.org/10.1021/acs.langmuir.8b02925.

Zhang, K., Jia, N., Liu, L., 2019a. CO_2 storage in fractured nanopores underground: phase behaviour study. Appl. Energy 238, 911–928. https://doi.org/10.1016/j.apenergy.2019.01.088.

Zhang, K., Jia, N., Liu, L., 2019b. Generalized critical shifts of confined fluids in nanopores with adsorptions. Chem. Eng. J. 372, 809–814. https://doi.org/10.1016/j.cej.2019.04.198.

Zhang, K., Tontiwachwuthikul, P., Jia, N., et al., 2019c. Four nanoscale-extended equations of state: phase behaviour of confined fluids in shale reservoirs. Fuel 250, 88–97. https://doi.org/10.1016/j.fuel.2019.03.095.

Zhu, Y., Su, H., Jing, Y., et al., 2016. Methane adsorption on the surface of a model of shale: A density functional theory study. Appl. Surf. Sci. 387, 379–384. https://doi.org/10.1016/j.apsusc.2016.06.033.